Table 3
The Proteoglycan and Hydroxyproline Content (Mean ± SD) and Correlation Coefficient With T_2, T_2^*, and dGEMRIC in Each ROI*

Cartilage matrix		ROI 1	ROI 2	ROI 3
Proteoglycan	Content (μg/mg)	57.0 ± 8.8	56.1 ± 10.1	55.9 ± 6.4
	Correlation with T_2	0.15	0.28	−0.24
	Correlation with T_2^*	0.28	0.15	−0.35
	Correlation with dGEMRIC	0.28	0.18	−0.27
Hydroxyproline	Content (μg/mg)	116.6 ± 12.4	116.9 ± 10.9	119.6 ± 10.8
	Correlation with T_2	0.20	0.21	0.21
	Correlation with T_2^*	0.20	0.03	−0.03
	Correlation with dGEMRIC	0.15	−0.65	−0.38

*No significant correlation between cartilage matrix and T_2/T_2^*/dGEMRIC values in all ROIs.

for T_2^*, and 166/244/277 msec for dGEMRIC values (Table 1). T_2, T_2^*, and dGEMRIC values in the anteriorly located zones (ROIs 2 and 3) had significantly higher values ($P < 0.05$) compared with those in the centrally located zone (ROI 1). Relative to the values at ROI 1, there was an increase of 22% at ROI 2 and 40% at ROI 3 on average T_2 values, an increase of 39% at ROI 2 and 61% at ROI 3 on average T_2^* values, and an increase of 47% at ROI 2 and 67% at ROI 3 on average dGEMRIC values. T_2 value was significantly correlated with that of T_2^*, with the correlation coefficient being 0.6 ($P < 0.01$) at ROI 1, 0.4 ($P < 0.05$) at ROI 2, and 0.6 ($P < 0.05$) at ROI 3. However, dGEMRIC value had no significant correlation with T_2 and T_2^* values at each zone.

The average proteoglycan and hydroxyproline content in each ROI was 57/56/56 μg/mg and 117/117/120 μg/mg, respectively (Table 3). There were no significant differences in the proteoglycan and hydroxyproline contents among ROIs, and these values were not correlated with T_2, T_2^*, and dGEMRIC values, using the Spearman correlation coefficient (Table 3).

At position B, T_2/T_2^*/dGEMRIC values increased by 24/44/31% at ROI 1 and decreased by 18/2.9/11% at ROI 3 on average compared with the values at position A (Table 1). There was a significant increase in the T_2 value at ROI 1 and the T_2^* value at ROIs 1 and 2 and a significant decrease in the T_2 value at ROI 3 ($P < 0.05$).

At position C, the T_2/T_2^*/dGEMRIC values increased by 6.8/11/0.8% at ROI 1 and decreased by 12/6.7/11% at ROI 3 on average compared with the values at position A (Table 2). There was no significant difference in the T_2/T_2^*/dGEMRIC values between positions A and C except a significant decrease in the T_2 value at ROI 3 ($P < 0.05$).

In the polarized light microscopy assessment, the cartilage of 6-month-old pigs had two zones with different birefringence intensity. As the birefringence is caused by a considerable influence of collagen network arrangement on the cartilage matrix structure, the result indicated that the porcine cartilage used in this study had anisotropic collagen structure (Fig. 3).

DISCUSSION

In biological tissues with highly ordered collagen, such as tendons and ligaments, strong parallel-oriented dipolar interactions of protons in water molecules binding to collagen make a significant contribution in dephasing the MR signal after excitation, resulting in shortened T_2 (16,17). The dipolar interactions are modulated by the angle between the vector joining the two spins and the external magnetic field and are minimized when the angle approaches 55° (called the magic angle), leading to a relative increase of T_2 compared with other angles of the direction. Quantitative MR evaluation of the articular cartilage is also subject to influence of the magic-angle effect, in accordance with the relative position between the collagen alignment of the cartilage and the direction of external magnetic field (18). The ultrastructure of a normal cartilage represents anisotropic collagen fiber architecture along its depth. The presence of 40–60% of deep cartilage represents predominantly parallel orientation of the fiber perpendicular to the subchondral plate (radial zone). The next 20–30% of the cartilage represents random orientation of the fiber (transitional zone). The thin superficial zone with 3–12% of the cartilage represents alignment of the collagen parallel to the articular surface (16). Previous experimental studies using excised cartilage specimen showed different magnitudes of the magic-angle effect, depending on the depth of the cartilage due to variability in the arrangement of collagen

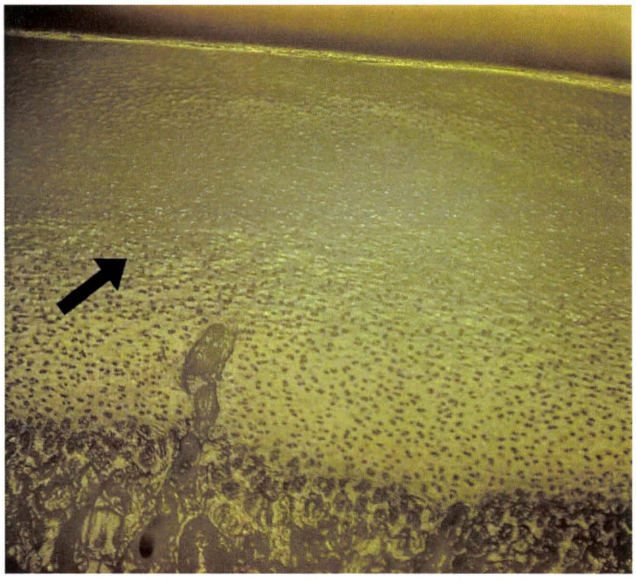

FIG. 3. Histological assessment of birefringence in 6-month-old porcine femoral cartilage specimens using polarized light microscopy. The cartilage samples were prepared as reported by Rieppo et al. (15) and Kiraly et al. (38). Decreased birefringence signal was shown in the superficial half of the cartilage (arrow).

fibers (19–22). On high-resolution T_2 maps of excised canine cartilage plugs, Xia et al. (19) found little orientation dependence of T_2 in the transitional zone, in contrast to the notable orientation dependence in the radial zone, with T_2 increasing by ~80% when the collagen fibers were aligned at 57° to B_0 compared with a 0° orientation. While evaluating the orientation effect on bulk cartilage T_2, Gründer et al. (22) observed the maximum increase in T_2 value when the radial zone was oriented at 55° to B_0, i.e., increasing by 300% compared with that at 0° orientation. To our knowledge, however, influence of the magic-angle effect on T_2 value has not been investigated with respect to the articular cartilage, using a more realistic joint model than the excised cartilage plugs.

In the present study, influence of the magic-angle effect on quantitative MR evaluation of the cartilage was investigated using en bloc knee joints retaining all intra-articular structures, the capsule, and the surrounding muscle. These animal knee joints were more realistic models than excised cartilage specimens. Intra-articular mechanical factors, which may have accelerating or competing effects on quantitative MR assessments in clinical MRI, cannot be investigated without using whole-knee models. Comparison of the MR assessments between positions A and C was aimed at evaluating the isolated influence of the magic-angle effect on the identical intra-articular biomechanical condition at an extended knee position. At position C, we expected that T_2 and T_2^* would increase at ROI 1 by changing the cartilage orientation more sensitive to the magic-angle effect and that those values would decrease at ROI 3 by changing the cartilage orientation less sensitive to the magic-angle effect. These expected tendencies were partly confirmed in our findings, with an increase of 6.8 and 11% at ROI 1 and a decrease of 12 and 6.7% at ROI 3 in T_2 and T_2^* values. However, the effect of orientation on cartilage was relatively small compared with that of previous findings using excised cartilage samples (19–22). With respect to dGEMRIC values, prior studies showed no orientational dependence of T_1 in the excised canine cartilage (19). The present findings also demonstrated a small change in the dGEMRIC value between positions A and C, with no significant difference.

MRI at knee flexion by 40° (position B) showed a more notable change in all examined parameters, resulting in a statistically significant difference in T_2 value at ROIs 1 and 3 and T_2^* value at ROI 1 and ROI 2. In comparison between positions A and B, the magnitudes of change at ROI 1 in T_2, T_2^*, and dGEMRIC values were more than three times greater than the changes observed in comparison between positions A and C. It is likely that factors other than the magic-angle effect also played an important role in the quantitative MR assessment changes associated with knee flexion. In the extended knee position, cartilage of ROI 1 is located in the weight-bearing portion of the femorotibial joint and is subject to relevant compressive and tensile force via interposed meniscus derived from preserved ligaments and the surrounding capsule. Cartilage of ROI 2 and ROI 3 is located in the non-weight-bearing portion of the femoral condyle and therefore is less subject to external compressed force. In the flexed knee position (position B), cartilage of ROI 1 was moved in the non-weight-bearing portion away from the meniscus, and the cartilage of ROI 3 was moved in the proximity of the patella-femoral joint. It is reasonable to consider that, according to knee flexion, the applied load-bearing force significantly decreased in the cartilage of ROI 1 and increased in the cartilage of ROI 3. Mesfar et al. (23) investigated the detailed biomechanics of knee joint during flexion movement by a three-dimensional computer-simulated technique and reported that tibiofemoral contact force was largest at full extension and decreased with joint flexion. Changes in the MR intensity and quantitative MR assessments in response to compressive loading were investigated thoroughly in experimental (9,24–26) and clinical studies (27–29). Rubenstein et al. (25) examined the MR appearance of an excised bovine cartilage under compressive force and observed a decrease in the signal intensity along the overall depth of the cartilage with a pressure of 1.10 MPa. In clinical MRI using a mechanical loading apparatus, significant decrease in the T_2 values was shown in the knee cartilage by loading 50–100% of the body weight during imaging (29,30). Decrease in the T_1 and T_2 values on loading has been accounted for by the deformation of cartilage architecture, extrusion of fluid content, and a relative increase in the proteoglycan and collagen content within the cartilage (25,27,28). Although changes in the pressure force on the cartilage were not directly measured in the present study, a significant increase in T_2 and T_2^* values at ROI 1 and decrease in T_2 values at ROI 3 by knee flexion were consistent with response to quantitative MR values due to the change in the biomechanical condition in the previous studies(23). In the present biochemical analysis, there was no difference of proteoglycan and hydroxyproline content among the three ROIs; however, T_2, T_2^*, and dGEMRIC values showed significant differences among the three ROIs. Although detailed zonal comparison along the cartilage depth was not conducted, lack of correlation between the quantitative MR values and the biochemical contents of the extracellular matrix may be partly accounted for by influence of localized biomechanical factors and/or the magic-angle effect. Mosher et al. (30) demonstrated a small difference in T_2 values between the cartilage zone orientated at 55° to B_0 and cartilage zone in parallel with B_0 in healthy volunteers and hypothesized that regional differences in the degree of cartilage compression are primarily responsible for the observed regional differences in the cartilage T_2. Our finding that T_2 measurement in the cartilage was influenced by both the magic-angle effect and localized biomechanical factors was in accordance with a previous clinical paper (30).

In the present study, we examined T_2, T_2^*, and dGEMRIC values as the major parameters in quantitative MR assessment of the cartilage. In prior ex vivo and in vivo studies, the T_2 value was assumed to be primarily correlated with water and collagen content or collagenous architecture (19,31), and the dGEMRIC value was assumed to be primarily sensitive to proteoglycan concentration within the cartilage (32). T_2^* assessment of the cartilage was studied in most recent investigations and assumed to be a potent alternative to T_2 assessment,

with faster scanning time (3). In spite of the assumed greater influence of the magic-angle effect on T_2 and T_2^* values than on T_1 value (17), the effect of orientational changes in the extended knee (position C) was similarly small in all three parameters. In knee flexion (position B), however, all three parameters showed a distinct increase at ROI 1, with the most pronounced change in T_2^* value. Although T_2 and T_2^* values were assumed to be sensitive to similar components of the cartilage and significant correlation between the two parameters was shown in our study, there may be considerable difference in sensitivity to the intracartilage component change and severity of other influential factors such as the magic-angle effect and susceptibility artifact around the bone–cartilage interface. Our results suggest that all three quantitative MR measurements may allow intra-articular biomechanical assessment in association with knee flexion. However, further studies are required to clarify the usefulness of individual MR parameters as a biomechanical surrogate.

Our study had several limitations. First, the small-diameter quadrature knee coil and gradient insert needed to perform the MR measurements did not allow the orientation of the femur to be varied by more than 40°. Therefore, MR measurements were not compared at two knee positions with a difference of the femoral shaft orientation around 55°, assuming it to present a maximum magic-angle effect. Change in the MR measurements of the articular cartilage at deep flexion, more than 40° in association with a different biomechanical condition of the intra-articular structures, was unknown. Second, the composition and thickness of the articular cartilage in different species may vary as a consequence of different load-bearing patterns, and the ex vivo whole-knee model did not incorporate surrounding muscle action such as contraction of the quadriceps or hamstrings or forces from surrounding ligamentous restraints. Severity and localization of change in the MR measurements, in association with knee flexion, may be different in human knee imaging in vivo. Third, although T_2, T_2^*, and dGEMRIC maps in this study were obtained with relatively high voxel resolution (voxel size 0.5 × 0.5 × 3.0 mm^3), the resolution is generally lower than that used in prior ex vivo studies. Because of the limited resolutions, assessment in layer-specific zones, such as superficial or deep layers of the cartilage, was not conducted in this study. The resultant volume-averaging effects might decrease the magnitude of the orientation effect. White et al. (33) assessed T_2 mapping characteristics of normal articular cartilage and of cartilage at sites of arthroscopic repair by in vivo imaging. Hannila et al. (34) assessed the topographical variation of T_2 relaxation time of articular cartilage in the young healthy knee joint. In these studies, MRI was performed using 1.5-T system and the voxel resolution was generally lower than in the present study. Juvenile porcine cartilage provided cartilage thickness similar to human adult cartilage. It is important to note that the resolution used in this study is similar to that used in high-resolution clinical imaging of the knee, and therefore our observations should be representative of the magnitude of the magic-angle effect that may be observed in routine clinical imaging. Fourth, previous histological investigations showed that immature pigs had less anisotropic collagen structure and different collagen fibril orientation with respect to the cartilage surface compared with matured pigs (15), and the 6-month-old porcine femoral cartilage in the present study was not matured yet. Using polarized light microscopy, however, we demonstrated that the 6-month-old porcine femoral cartilage had two zones with different anisotropy relating with collagen content and organization. Gründer et al. (9) showed the anisotropic zones determined by the arrangement of the collagenous network fibers of cartilage in juvenile animals. From our histological finding and those previous reports, we considered that the cartilage of juvenile pigs had certainly two zones with different anisotropy. Furthermore, it is important to clarify how T_2/T_2^*/dGEMRIC values in each layer would change at different positions; however, assessment in layer-specific zones was not conducted in this study due to the aforementioned limited resolution. The juvenile porcine cartilage might have less anisotropic collagenous structure and different collagen fibril orientation compared with mature porcine cartilage and human cartilage, and differences of magic-angle effect and change of quantitative MR assessments among examined species were unknown. Finally, we used freezing and thawing management in cadaver knees according to previous papers that reported freezing does not affect the material properties of cartilage (35,36). In contrast, Laouar et al. (37) showed that ice formation during cooling and warming of intact porcine articular cartilage caused a loss of fixed charged density throughout the articular cartilage matrix, reflecting changes in the content or structure of the proteoglycan component of the matrix. It is possible that freezing and thawing of cadaver knees affected collagen fiber orientation in cartilage, which is different from the clinical situation.

In conclusion, results of this study indicate that the effect of orientation on cartilage T_2 and T_2^* values in juvenile pigs is substantially less than that predicted on the basis of prior ex vivo studies. Substantial changes in T_2, T_2^*, and dGEMRIC values were demonstrated in response to knee flexion, presumably due to a change in the intra-articular biomechanical environment. After excluding the factor of the magic-angle effect, our results may suggest that quantitative MR measurements allow intra-articular biomechanical assessments in association with kinematic knee imaging.

ACKNOWLEDGMENTS

The authors thank Norinao Matsumoto and Yoshihiro Sakaguchi at the Matsumoto Medical Clinic and Yasuo Hara at the Department of Technology Development, IVTeC, Japan, for their technical assistance.

REFERENCES

1. Mosher TJ, Dardzinski BJ, Smith MB. Human articular cartilage: Influence of aging and early symptomatic degeneration on the spatial variation of T2-preliminary findings at 3 T. Radiology 2000;214: 259–266.
2. Dunn TC, Lu Y, Jin H, Ries MD, Majumdar S. T2 relaxation time of cartilage at MR imaging: comparison with severity of knee osteoarthritis. Radiology 2004;232:592–598.

3. Welsch GH, Mamisch TC, Hughes T, Zilkens C, Quirbach S, Scheffler K, Kraff O, Schweitzer ME, Szomolanyi P, Trattnig S. In vivo biochemical 7.0 tesla magnetic resonance: preliminary results of dGEMRIC, zonal T2, and T2* mapping of articular cartilage. Invest Radiol 2008;43:619–626.
4. Lammentausta E, Kiviranta P, Nissi MJ, Laasanen MS, Kiviranta I, Nieminen MT, Jurvelin JS. T_2 relaxation time and delayed gadolinium-enhanced MRI of cartilage (dGEMRIC) of human patellar cartilage at 1.5 T and 9.4 T: relationships with tissue mechanical properties. J Orthop Res 2006;24:366–374.
5. Burstein D, Velyvis J, Scott KT, Stock KW, Kim YJ, Jaramillo D, Boutin RD, Gray ML. Protocol issues for delayed $Gd(DTPA)^{2-}$-enhanced MRI (dGEMRIC) for clinical evaluation of articular cartilage. Magn Reson Med 2001;45:36–41.
6. Li X, Benjamin Ma C, Link TM, Castillo DD, Blumenkrantz G, Lozano J, Carballido-Gamio J, Ries M, Majumdar S. In vivo $T_{1\rho}$ and T_2 mapping of articular cartilage in osteoarthritis of the knee using 3T MRI. Osteoarthritis Cartilage 2007;15:789–797.
7. Scarvell JM, Smith PN, Refshauge KM, Galloway HR, Woods KR. Comparison of kinematic analysis by mapping tibiofemoral contact with movement of the femoral condylar centres in healthy and anterior cruciate ligament injured knees. J Orthop Res 2004;22:955–962.
8. Li G, Moses JM, Papannagari R, Pathare NP, DeFrate LE, Gill TJ. Anterior cruciate ligament deficiency alters the in vivo motion of the tibiofemoral cartilage contact points in both the anteroposterior and mediolateral directions. J Bone Joint Surg Am 2006;88:1826–1834.
9. Gründer W, Kanowski M, Wagner M, Werner A. Visualization of pressure distribution within loaded joint cartilage by application of angle-sensitive NMR microscopy. Magn Reson Med 2000;43:884–891.
10. Liess C, Lüsse S, Karger N, Heller M, Glüer CC. Detection of changes in cartilage water content using MRI T2-mapping in vivo. Osteoarthritis Cartilage 2002;10:907–913.
11. Mosher TJ, Smith HE, Collins C, Liu Y, Hancy J, Dardzinski BJ, Smith MB. Change in knee cartilage T2 at MR imaging after running: a feasibility study. Radiology 2005;234:245–249.
12. Rubenstein JD, Kim JK, Morova-Protzner I, Stanchev PL, Henkelman RM. Effects of collagen orientation on MR imaging characteristics of bovine articular cartilage. Radiology 1993;188:219–226.
13. Kurkijärvi JE, Nissi MJ, Rieppo J, Töyräs J, Kiviranta I, Nieminen MT, Jurvelin JS. The zonal architecture of human articular cartilage described by T2 relaxation time in the presence of $Gd\text{-}DTPA^{2-}$. Magn Reson Imaging 2008;26:602–608.
14. Nieminen MT, Rieppo J, Silvennoinen J, Töyräs J, Hakumäki JM, Hyttinen MM, Helminen J, Jurvelin JS. Spatial assessment of articular cartilage proteoglycans with Gd-DTPA-enhanced T1 imaging. Magn Reson Med 2002;48:640–648.
15. Rieppo J, Hyttinen MM, Halmesmaki E, Ruotsalainen H, Vasara A, Kiviranta I, Jurvelin JS, Helminen HJ. Changes in spatial collagen content and collagen network architecture in porcine articular cartilage during growth and maturation. Osteoarthritis Cartilage 2009;17:448–455.
16. Xia Y. Magic-angle effect in magnetic resonance imaging of articular cartilage: A review. Invest Radiol 2000;35:602–621.
17. Bydder M, Rahal A, Fullerton GD, Bydder GM. The magic angle effect: a source of artifact, determinant of image contrast, and technique for imaging. J Magn Reson Imaging 2007;25:290–300.
18. Peto S, Gillis P. Fiber-to-field angle dependence of proton nuclear magnetic relaxation in collagen. Magn Reson Imaging 1990;8:705–712.
19. Xia Y. Relaxation anisotropy in cartilage by NMR microscopy (muMRI) at 14-microm resolution. Magn Reson Med 1998;39:941–949.
20. Goodwin DW, Zhu H, Dunn JF. In vitro MR imaging of hyaline cartilage: correlation with scanning electron microscopy. AJR Am J Roentgenol 2000;174:405–409.
21. Mlynarik V, Degrassi A, Toffanin R, Vittur F, Cova M, Pozzi-Mucelli RS. Investigation of laminar appearance of articular cartilage by means of magnetic resonance microscopy. Magn Reson Imaging 1996;14:435–442.
22. Gründer W, Wagner M, Werner A. MR-microscopic visualization of anisotropic internal cartilage structures using the magic angle technique. Magn Reson Med 1998;39:376–382.
23. Mesfar W, Shirazi-Adl A. Computational biomechanics of knee joint in open kinetic chain extension exercises. Comp Methods Biomech Biomed Eng 2008;11:55–61.
24. Kaufman JH, Regatte RR, Bolinger L, Kneeland JB, Reddy R, Leigh JS. A novel approach to observing articular cartilage deformation in vitro via magnetic resonance imaging. J Magn Reson Imaging 1999;9:653–662.
25. Rubenstein JD, Kim JK, Henkelman RM. Effects of compression and recovery on bovine articular cartilage: appearance on MR images. Radiology 1996;201:843–850.
26. Wayne JS, Kraft KA, Shields KJ, Yin C, Owen JR, Disler DG. MR imaging of normal and matrix-depleted cartilage: correlation with biomechanical function and biochemical composition. Radiology 2003;228:493–499.
27. Liess C, Lüsse S, Karger N, Heller M, Glüer CC. Detection of changes in cartilage water content using MRI T_2-mapping in vivo. Osteoarthritis Cartilage 2002;10:907–913.
28. Nishii T, Kuroda K, Matsuoka Y, Sahara T, Yoshikawa H. Change in knee cartilage T_2 in response to mechanical loading. J Magn Reson Imaging 2008;28:175–180.
29. Nag D, Liney GP, Gillespie P, Sherman KP. Quantification of T_2 relaxation changes in articular cartilage with in situ mechanical loading of the knee. J Magn Reson Imaging 2004;19:317–322.
30. Mosher TJ, Smith H, Dardzinski BJ, Schmithorst VJ, Smith MB. MR imaging and T_2 mapping of femoral cartilage: in vivo determination of the magic angle effect. AJR Am J Roentgenol 2001;177:665–669.
31. Xia Y, Moody JB, Alhadlaq H. Orientational dependence of T_2 relaxation in articular cartilage: a microscopic MRI (microMRI) study. Magn Reson Med 2002;48:460–469.
32. Bashir A, Gray ML, Hartke J, Burstein D. Nondestructive imaging of human cartilage glycosaminoglycan concentration by MRI. Magn Reson Med 1999;41:857–865.
33. White LM, Sussman MS, Hurtig M, Probyn L, Tomlinson G, Kandel R. Cartilage T_2 assessment: differentiation of normal hyaline cartilage and reparative tissue after arthroscopic cartilage repair in equine subjects. Radiology 2006;241:407–414.
34. Hannila I, Räinä SS, Tervonen O, Ojala R, Nieminen MT. Topographical variation of T_2 relaxation time in the young adult knee cartilage at 1.5T. Osteoarthritis Cartilage 2009;17:1570–1575.
35. Kempson GE, Spivey CJ, Swanson SV, Freeman MR. Patterns of cartilage stiffness on normal and degenerate human femoral heads. J Biomech 1971;4:597–609.
36. Samosky JT, Burstein D, Grimson WE, Howe R, Martin S, Gray ML. Spatially-localized correlation of dGEMRIC-measured GAG distribution and mechanical stiffness in the human tibial plateau. J Orthop Res 2005;23:93–101.
37. Laouar L, Fishbein K, McGann LE, Horton WE, Spencer RG, Jomha NM. Cryopreservation of porcine articular cartilage: MRI and biochemical results after different freezing protocols. Cryobiology 2007;54:36–43.
38. Kiraly K, Hyttinen MM, Lapveteläinen T, Elo M, Kiviranta I, Dobai J, Modis L, Helminen HJ, Arokoski PA. Specimen preparation and quantification of collagen birefringence in unstained sections of articular cartilage using image analysis and polarizing light microscopy. Histochem J 1997;29:317–327.

Direct Anterior Cruciate Ligament Insertion to the Femur Assessed by Histology and 3-Dimensional Volume-Rendered Computed Tomography

Takehiko Iwahashi, M.D., Ph.D., Konsei Shino, M.D., Ph.D., Ken Nakata, M.D., Ph.D., Hidenori Otsubo, M.D., Tomoyuki Suzuki, M.D., Hiroshi Amano, M.D., and Norimasa Nakamura, M.D., Ph.D.

Purpose: The purpose of this study was to histologically identify the direct and indirect insertion of the femoral anterior cruciate ligament (ACL) insertion. Furthermore, we quantitatively measured the direct femoral insertion area by use of the 3-dimensional (3D) volume-rendered (VR) computed tomography (CT) model. **Methods:** By use of 8 intact cadaveric knees, the lateral femoral condyle including the ACL attachment was sectioned for histologic examination in 3 oblique-axial planes parallel to the roof of the intercondylar notch and in the sagittal planes. Before sectioning, these knees had been subjected to CT to obtain 3D VR images of the femur. Once the direct insertion of the ACL was identified on each histologic section, the corresponding image was superimposed on the corresponding CT image. **Results:** The direct ACL insertion, in which dense collagen fibers were connected to the bone by the fibrocartilaginous layer, was microscopically identified at the region between the posteromedial articular cartilage margin of the lateral femoral condyle and the linear bony ridge 7 to 10 mm anterior to the articular cartilage margin. Meticulous comparison of histologic analysis and the 3D VR CT model showed that the ACL direct insertion coincided with a crescent-shaped hollow just behind the linear bony ridge. The direct insertion measured 17.4 ± 0.9 mm (mean ± SD) in length, 8.0 ± 0.5 mm in width, and 128.3 ± 10.5 mm^2 in area. **Conclusions:** The direct insertion of the ACL is located in the depression between the resident's ridge and the articular cartilage margin on the lateral femoral condyle. It measured 17.4 ± 0.9 mm in length, 8.0 ± 0.5 mm in width, and 128.3 ± 10.5 mm^2 in area. **Clinical Relevance:** Delineation of the ACL femoral direct insertion by 3D VR CT could be a useful tool for planning of accurate femoral tunnel positioning in anatomic ACL reconstruction.

Ligaments are discrete bands of dense connective tissue that span joints and connect bones and thus serve an important role in both stabilizing joints and guiding joint motion. Ligaments have 2 unique modes of insertion to the bone, namely direct insertion and indirect insertion. Direct insertion has a zonal architecture including the transition from ligamentous tissue, noncalcified cartilage, and calcified cartilage to bone, which allows for a gradual force distribution and differential tensioning of all inserting components into the insertion site.[1,2] The indirect type of insertion has a significantly simpler ultrastructure, where the ligament directly anchors to the bone by collagen fibers without forming a clear transitional zone. These fibers represent the equivalent to the collagen fibers anchoring the periosteum to bone as described by Benjamin.[3] The direct insertion type represents a firm and fixed attachment allowing for a gradual load distribution into the subchon-

From the Department of Orthopaedics (T.I., K.N., H.A., N.N.), Osaka University Graduate School of Medicine, Osaka; Faculty of Comprehensive Rehabilitation (K.S.), Osaka Prefecture University, Osaka; and Department of Orthopaedics (H.O., T.S.), Sapporo Medical University, Sapporo, Japan.

The authors report no conflict of interest.

Received November 19, 2008; accepted January 26, 2010.

Address correspondence and reprint requests to Takehiko Iwahashi, M.D., Ph.D., Department of Orthopaedics, Osaka University Graduate School of Medicine, 2-2 Yamadaoka, Suita, Osaka 565-0871, Japan. E-mail: tiwa1884@yahoo.co.jp

0749-8063/8659/$36.00

doi:10.1016/j.arthro.2010.01.023

dral bone and, from a biomechanical point of view, is thus extremely important as a key link between the ligament and bone to transmit mechanical load to the joint.[4]

Several studies have reported on the anterior cruciate ligament (ACL) femoral attachment area by macroscopic observation[5-14]; however, such studies only identified the overall profile of the femoral attachment area of the ACL. In contrast, there have been a limited number of studies that microscopically analyzed the femoral insertion of the ACL, and no study has specifically identified the area of the direct femoral insertion of the ACL. Ferretti et al.[6] performed a histologic examination of the ACL femoral footprint, but they only referred to the lateral bifurcate ridge without evaluation of the insertion site.

Ferretti et al.[6] also quantitatively showed the landmarks of the femoral attachment of the ACL by 3-dimensional (3D) modeling using a 3D laser digitizer. Because 3D images obtained by the 3D laser digitizer theoretically delineate the traced surface figure,[15] the 3D modeling of the femoral attachment in their study might not have accurately delineated the bony surface because of potential contamination of surface soft tissue. In this regard, it is known that 3D volume-rendered (VR) computed tomography (CT) can accurately delineate the surface of any bony structure.[16,17]

The purposes of our study were to histologically identify the direct and indirect insertion of the femoral ACL attachment area and to quantify the direct insertion area by superimposing the microscopic anatomy of the region onto the 3D VR CT model of the femoral condyle.

The hypotheses of this study were that (1) there may be a direct insertion type microscopically identified inside the ACL femoral attachment area and (2) the direct insertion area may be delineated by a bony surface landmark.

METHODS

We obtained 8 ACL-intact knees (4 paired knees) from 4 embalmed cadavers (3 men and 1 woman aged between 66 and 87 years, with a mean age of 77 years) with a height of 151 to 170 cm (mean ± SD, 162 ± 8.0 cm) for this study. The cadavers were fixed in 8% formalin and preserved in 30% ethanol. The muscle around the knee joint, as well as the capsular ligament with patella, was removed to allow thorough examination of the interior of the joint. The posterior cruciate ligament was also removed. Then, the ACL was detached from the tibial attachment.

The femur was cut at 15 cm from the joint surface and was longitudinally split with an oscillating saw in the sagittal plane, including the highest point of the anterior outlet of the intercondylar notch.

Macroscopic Observation of ACL Femoral Footprint

The ACL femoral footprint was macroscopically analyzed to determine the extent of ligament fiber distribution by pulling the ACL in the anteroinferior or posterosuperior direction parallel to the roof of the notch.

CT Scanning and Image Reconstruction

CT scans of the femur were taken under the conditions of 120 kV, 100 mA, and a 1-mm slice thickness (ProSpeed AI system; GE Healthcare, Waukesha, WI).

The CT data were processed with software for image analysis (Virtual Place-M; AZE, Tokyo, Japan), and the femoral contour was automatically extracted from the images (segmentation). A 3D bone surface model was constructed by the marching cube technique. The images were made up of numerous tiny triangles, each of which contained the positional data for 3 points. Reconstructed images were viewed by use of a modified version of Visualization Tool Kit (VTK) software (Kitware, Clifton Park, NY). Specifically, CT images of the lateral femoral condyle along the oblique-axial planes parallel to the roof of the notch, identical to the sections for histologic analysis (slices 1, 2, and 3), were made (Fig 1A). A plane parallel to the medial aspect of the lateral femoral condyle was also generated (Fig 1B).

Histologic Examination of ACL Attachment Area to Femur

All 8 lateral femoral condyles, with preservation of the ACL femoral footprint, were decalcified in hydrochloric acid and embedded in paraffin for light microscopy. We cut 4 specimens from the 4 cadavers into 3 blocks of even thickness along the oblique-axial planes parallel to the roof of the notch, and their sections were sliced into 5-μm specimens, stained with H&E, and observed under a microscope (Nikon ECLIPSE 90i; Nikon, Melville, NY) at a magnification of ×40 to meticulously indentify the attachment area including the insertion of dense collagen fibers and surrounding coarse fibrous tissues (Fig 1A, slices 1, 2, and 3). For quantification of the insertion area, the anteroposterior distance on the medial aspect of the lateral femoral condyle in slices 1, 2, and 3 was measured with a slide caliper under a microscope.

The remaining 4 specimens were cut at the level of the attachment area along the sagittal plane, sliced into

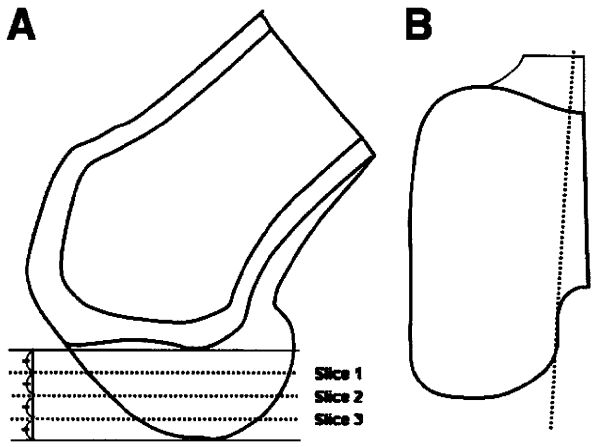

FIGURE 1. Demographic description of section planes for histologic analysis. (A) The lateral femoral condyle is cut into 4 blocks at even intervals along the oblique-axial planes parallel to the roof of the notch, and the superior-anterior section (slice 1), middle section (slice 2), and inferior-posterior section (slice 3) are subjected to histologic analysis. (B) The lateral femoral condyle is cut at the level of the attachment area along the sagittal plane to perpendicularly determine the ligament attachment area.

5-μm specimens, stained with hematoxylin, and observed under a light microscope (Fig 1B). Histologic analysis was performed by 3 orthopaedic surgeons (T.I., H.O., and T.S.).

Superimposition of CT Images on Histologic Data

Comparison of Histologic Preparations and Slices From 3D VR CT Model: Each of the histologic slices (slices 1, 2, and 3) was compared with the corresponding CT images to assess the bony surface morphology around the direct insertion of the ACL. First, the area of direct insertion of the ACL on the lateral femoral condyle was measured on microscopic histologic images of slices 1, 2, and 3 with slide calipers. Then, the histologic image of each slice was superimposed on the CT model image of the corresponding slice to project the ACL femoral attachment area. The dimensions of the attachment area were measured on the reconstructed slices from the 3D VR CT model.

Evaluation of Position and Area of Direct Insertion of ACL by 3D VR CT Model: On the basis of the microscopic data, the region of the direct insertion of the ACL was superimposed on the slices from the 3D VR CT model. The area of the direct insertion of the ACL was calculated on the 3D VR CT model by use of computer software (Kitware).

RESULTS

Macroscopic Observation of ACL Femoral Attachment Area and Bony Surface Around Area

The ACL fibers ran anteriorly-inferiorly, parallel to the roof of the intercondylar notch (Fig 2A). Obviously, the attachments were located in the posterior-superior quarter of the lateral wall of the notch. Although the whole attachment area was apparently broad with an oval shape (Fig 2B), when the dense fiber of the ACL substance (Fig 2E) was inverted posteriorly-superiorly to observe the anterior border of its attachment area, it was found that the border formed a linear line demarcating the posterior-superior quarter of the lateral wall of the notch, extending to a line comprising the posterior cortical border of the femoral diaphysis (Fig 2B). The posterior surface of the ACL attachment area extended to the cartilage margin of the lateral femoral condyle (Fig 2C). The dense fibrous tissue of the ACL inserted into the concave area (Fig 2D) located in the very distant portion of the lateral wall of the notch.

Microscopic Findings of ACL Attachment Area to Femur

Observation from either the oblique axial planes parallel to the roof of the notch (Fig 3A) or sagittal planes (Fig 3B) showed that the linear bony ridge formed the anterior-inferior rim of the dense collagen fiber attachment of the ACL (Fig 3A, large arrow). The femoral attachment area extended posteriorly and superiorly to the articular cartilage margin (Fig 3A, small arrows). Observation by the oblique axial planes parallel to the roof of the notch enabled the delineation of the central dense collagen fibers (Fig 3A, oval) from the attachment of the surrounding coarse fibrous tissues. The dense collagen fibers directly inserted into the concave area (Fig 3A, arrowheads) behind the bony ridge (Fig 3A, large arrow), whereas coarse fibrous tissues attached to the bone just anterior to the bony ridge or the concavity. A higher-magnification view showed that the attachment area of the coarse fibrous tissue surrounded the dense fiber attachment area extending anteriorly over the bony ridge (Fig 3C). It also showed that the dense fibers attached to the bone by direct insertion with the zonal transition from ligamentous tissue, noncalcified cartilage, and calcified cartilage to bone (Figs 3D, 3G, and 3H).

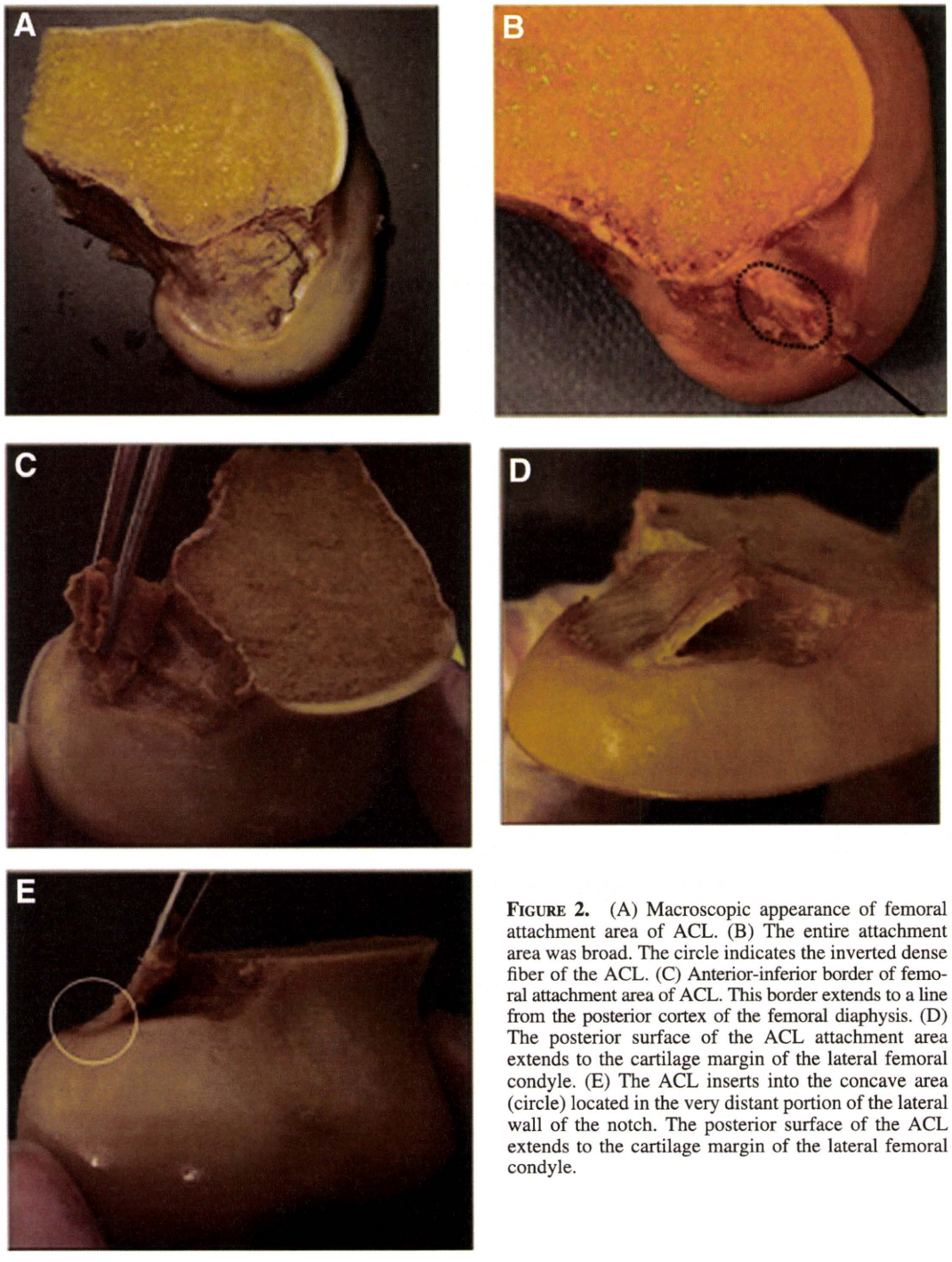

FIGURE 2. (A) Macroscopic appearance of femoral attachment area of ACL. (B) The entire attachment area was broad. The circle indicates the inverted dense fiber of the ACL. (C) Anterior-inferior border of femoral attachment area of ACL. This border extends to a line from the posterior cortex of the femoral diaphysis. (D) The posterior surface of the ACL attachment area extends to the cartilage margin of the lateral femoral condyle. (E) The ACL inserts into the concave area (circle) located in the very distant portion of the lateral wall of the notch. The posterior surface of the ACL extends to the cartilage margin of the lateral femoral condyle.

On the other hand, in the region adjacent to the direct insertion area, the coarse fibrous tissues attached to the bone through indirect insertion without the cartilaginous transition zones (Figs 3C, 3E, 3F, and 3I).

Quantitative Evaluation of Direct Insertion of ACL by Histology and 3D VR CT

Comparison of Histology With CT Image: On both the histologic images and the 3D VR CT images, an elevated bony ridge was observed in the anterior

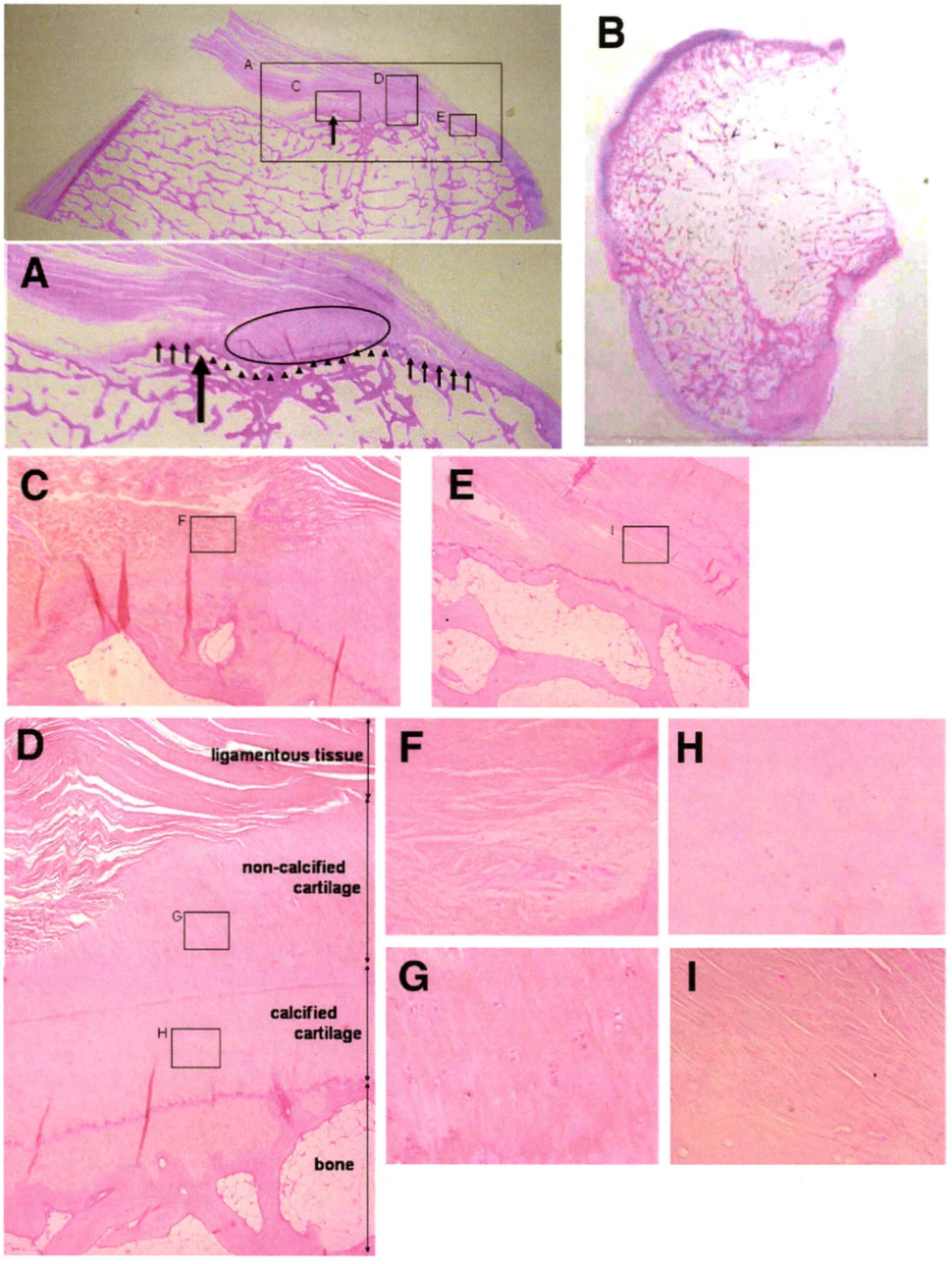

FIGURE 3. Histology of ACL attachment area to lateral femoral condyle (H&E stain). (A) Section from oblique axial plane parallel to roof of notch (original magnification ×5). The presence of bony prominence is confirmed (large arrow) adjacent to the anterior border of the concave area (arrowheads), and central dense collagenous fibers (oval) insert into the concave area behind the bony ridge. The coarse fibrous region is surrounded by the central dense collagenous fibers and attached to the bone around the bony ridge and the concavity (small arrows). The coarse fibrous region extended posteriorly in contact with the margin of the articular cartilage. (B) Schematic diagram of direct insertion area of ACL attachment area on lateral femoral condyle (sagittal plane through medial part of lateral condyle) (original magnification ×5). (C) Higher-magnification view of attachment area of coarse fibrous region around bony ridge (original magnification ×40). There are no cartilaginous transition zones, and the indirect insertion is developed. (D) Higher-magnification view of attachment area of central dense collagenous fibers to bone (original magnification ×40). (E) Higher-magnification view of coarse fibrous region extending posteriorly in contact with margin of articular cartilage (original magnification ×40). (F) Higher-magnification view of attachment area of coarse fibrous region around bony ridge (original magnification ×400). There are no cartilaginous transition zones, and the indirect insertion is developed. (G) Higher-magnification view of noncalcified cartilage in direct insertion (original magnification ×400). (H) Higher-magnification view of calcified cartilage in direct insertion (original magnification ×400). The direct insertion, which represented the transition from ligamentous tissue, noncalcified cartilage, and calcified cartilage to bone, is conformed. (I) Higher-magnification view of attachment area of coarse fibrous region extending posteriorly in contact with margin of articular cartilage (original magnification ×400). There are no cartilaginous transition zones, and the indirect insertion is developed.

margin of the direct insertion of the ACL. The 3D VR CT model reproduced the characteristic bony surface morphology of the concave area that extended from the bony elevation to the posterior margin of the medial aspect of the lateral femoral condyle (Fig 4). Notably, close comparison of the histology with the CT images showed that the concave area in the medial aspect of the lateral femoral condyle on the CT images corresponded with the region of direct insertion of the ACL observed in the histologic sections. The antero-posterior width of the concave area was calculated as 7.9 ± 0.9 mm (mean ± SD) by CT and 7.8 ± 1.0 mm by histology at the slice 1 level. The width was calculated as 9.6 ± 0.7 mm by CT and 9.5 ± 0.6 mm by histology at the slice 2 level and 8.9 ± 0.8 mm by CT and 8.6 ± 0.5 mm by histology at the slice 3 level (Fig 5). The results are summarized in Table 1. With regard to the reliability of measurements made by CT and histology, the SDs and coefficients of variation for intraobserver and interobserver variability are shown in Table 2.

Location and Area of Collagenous ACL Fiber Insertion on 3D VR CT Images: The concavity observed on the 3D VR CT images was 17.4 ± 0.9 mm (mean ± SD) in length, 8.0 ± 0.5 mm in width, and 128.3 ± 10.5 mm^2 in area (Fig 4). The other measured data are listed in Table 3.

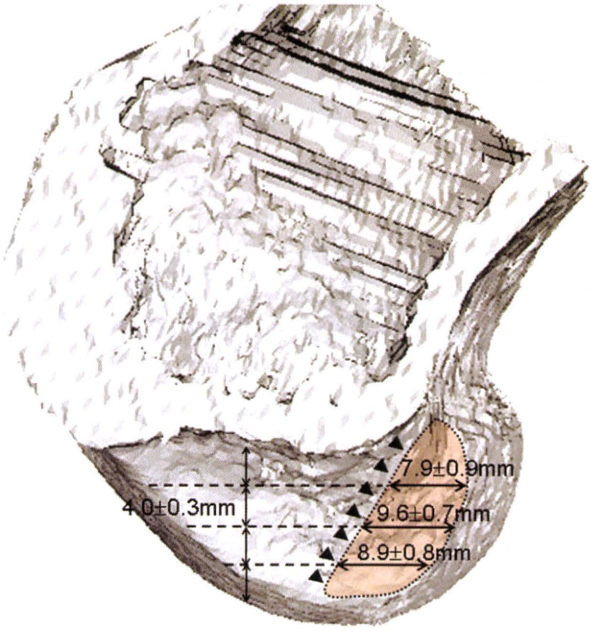

FIGURE 4. Three-dimensional VR CT model of lateral femoral condyle. The resident's ridge (arrowheads) is located proximal-distal along the entire ACL attachment.

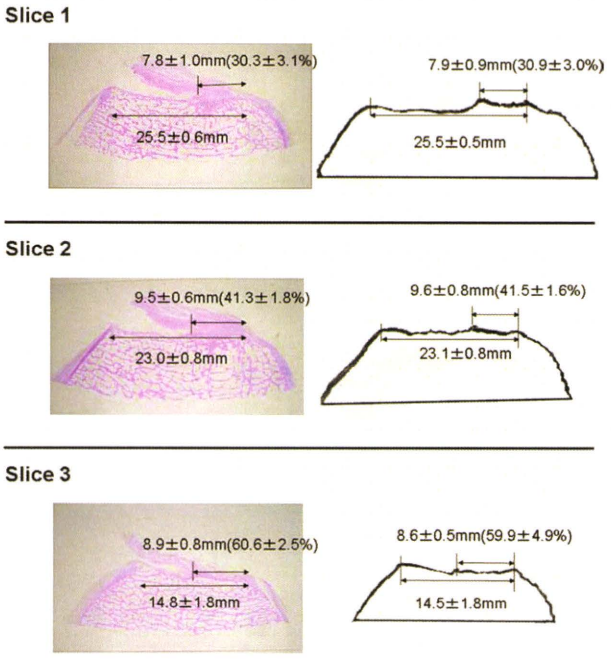

FIGURE 5. Semi-quantification of area of ACL attachment area on lateral femoral condyle by oblique axial planes parallel to roof of notch (corresponding to slices 1, 2, and 3 in Fig 1A). The ACL attachment area occupies 30.3% ± 3.1% (mean ± SD) in the superior-anterior sections, 41.3% ± 1.8% in the middle sections, and 60.6% ± 2.5% in the inferior-posterior sections. H&E stain, original magnification ×0.7.

DISCUSSION

Although the concept of anatomic reconstruction has been a trend in ACL reconstruction,[5,18] the definition of the term "anatomic" is not yet well defined. This may be mainly because of inconsistency in the definition of the geographic location of the ACL in-

TABLE 1. *Quantitative Evaluation of Region for Direct Insertion of ACL by Histology and Region of Depressed Area on 3D VR CT Model*

	Histology		CT Model	
	Mean	Range	Mean	Range
Length of lateral femoral condyle (mm)				
Slice 1	25.5 ± 0.6	25-26	25.5 ± 0.5	24.9-26.1
Slice 2	23.0 ± 0.8	22-24	23.1 ± 0.8	22.3-24.1
Slice 3	14.5 ± 1.7	13-17	14.8 ± 1.8	12.9-17.1
Footprint length (mm)				
Slice 1	7.8 ± 1.0	7-9	7.9 ± 0.9	7.1-8.8
Slice 2	9.5 ± 0.6	9-10	9.6 ± 0.7	8.8-10.3
Slice 3	8.6 ± 0.5	8-10	8.9 ± 0.8	7.9-9.7

TABLE 2. *Intraobserver and Interobserver SDs and Coefficients of Variation for 6 Parameters on Histologic or CT Evaluation*

	Histology				CT Model			
	Intraobserver		Interobserver		Intraobserver		Interobserver	
	SD (mm)	CV (%)	SD (mm)	CV (%)	SD (mm)	CV (%)	SD (mm)	CV (%)
Length of lateral femoral condyle								
Slice 1	0.6	2.3	0.6	2.3	0.5	2.1	0.5	2.1
Slice 2	0.0	0.0	0.6	2.4	0.3	1.3	0.6	2.3
Slice 3	0.6	3.3	0.0	0.0	0.6	3.5	0.4	2.1
Footprint length								
Slice 1	0.0	0.0	0.6	6.2	0.3	1.2	0.4	4.1
Slice 2	0.6	5.6	0.0	0.0	0.6	3.6	0.4	2.4
Slice 3	0.6	6.2	0.0	0.0	0.5	4.2	0.3	1.3

Abbreviations: CV, coefficient of variation.

sertion to the lateral femoral condyle.[5-14] In this study we have identified that the ACL insertion consists of 2 different structures, the direct insertion and the indirect insertion, by histologic analysis. Previous studies suggested that the direct insertion plays a major role in the mechanical link between the ligament and bone as compared with the indirect insertion,[1,2,7] and therefore, in anatomic ACL reconstruction, it may be reasonable to create the femoral tunnels within the direct insertion area. However, by macroscopic observation, it was impossible to distinguish the direct and indirect insertions. If one takes into account that most previous studies to identify the femoral footprint of the ACL have been done by macroscopic observation,[5-14] there is the potential risk of dismissing the relative ratio of functional importance between the direct and indirect insertions within the ACL footprint, which might be misleading with regard to the recommended geographic location of the femoral bone tunnels at the time of anatomic ACL reconstruction.

Notably, the bony surface of the direct insertion showed a concavity, and there was a prominence of the bony ridge adjacent to the anterior border of this concavity. This bony ridge geographically coincides with the "resident's ridge" proposed by Clancy and colleagues.[17] Hutchinson and Ash[19] also reported the existence of the resident's ridge at the anterior rim of the ACL attachment site, based on the results of microscopic investigation. Our macroscopic and microscopic observations showed that the ridge described by Hutchinson and Ash corresponds to the osseous elevation that was detected adjacent to the anterior border of the ACL direct insertion.

TABLE 3. *Two-Dimensional Measurements of ACL Direct Insertion*

	Mean	Range
Footprint length (mm)	17.4 ± 0.9	16.2-18.4
Footprint width (mm)	8.0 ± 0.5	7.1-8.3
Length of resident's ridge (mm)	14.5 ± 0.9	13.2-15.3
Height of resident's ridge (mm)	0.8 ± 0.1	0.7-0.9
Footprint area (mm^2)	128.3 ± 10.5	113.6-137.5

Previous reports on the location of the ACL attachment, including those of Colombet et al.[10] and Amis and Jakob,[8] indicated that the ACL attached to the lateral condyle of the femur at a site posterior to a line extending from the posterior cortex of the femoral diaphysis. Girgis et al.[11] reported that the ACL attachment area on the lateral femoral condyle was semicircular with a posterior bulge and a linear anterior rim. A more recent study by Purnell et al.[17] using high-resolution VR CT showed the relation between the ACL femoral attachment and the resident's ridge, as well as its location. The location of the ACL attachment and the resident's ridge reported in their study was exactly identical to that of the direct ACL insertion area presented in our study.

Ferretti et al.[6] also quantitatively reported on the 3D landmarks of the femoral attachment of the ACL using a 3D laser digitizer. The 3D laser digitizer theoretically traces the surface geometry of the specimen of interest and could potentially include the surface soft-tissue structures, and thus the image does not represent the bony surface landscape.[15] In fact, the area of ACL attachment area reported by Ferretti et al. was 196 mm^2, much larger than that observed in our study

(128 mm^2). If one takes into account that our 3D VR CT image accurately represents the bony surface landscape, such discrepancy might be attributed to the inclusion of the surface soft tissues in their study.[6] Furthermore, in terms of clinical implications, 3D VR CT has the advantage over the 3D laser digitizer, in that 3D VR CT can be applied to every patient clinically without an invasive procedure, and thus the 3D evaluation of the bony landmark to identify the ACL direct insertion can serve as a very useful tool for preoperative planning.

The limitation of this study was that we did not specifically observe the insertion of the separate bundles (anteromedial or posterolateral). However, the information about the location of the direct insertion of the ACL, which plays a pivotal biomechanical function, could be beneficial to the performance of anatomic and functional ACL reconstruction surgery. For anatomic reconstruction of the ACL, it is recommended to create a bone tunnel within the area we described by 3D VR CT as the direct attachment area or insertion in Fig 5. We believe that the bony surface landmark identified in this study could be helpful in all "anatomic" ACL reconstruction procedures regardless of the number of femoral tunnels (single or double) or the choice of graft materials.

CONCLUSIONS

The direct insertion of the ACL is located in the depression between the resident's ridge and the articular cartilage margin on the lateral femoral condyle. It measured 17.4 ± 0.9 mm in length, 8.0 ± 0.5 mm in width, and 128.3 ± 10.5 mm^2 in area.

REFERENCES

1. Schneider H. Structure of tendon attachments. *Z Anat Entwicklungsgesch* 1956;119:431-456 (in German).
2. Weiler A, Scheffler S. Healing of ligament and tendon to bone. In: Walsh WR, ed. *Orthopedic biology and medicine: Repair and regeneration of ligaments, tendons, and joint capsule.* Totowa, NJ, Humana Press, 2005;201-231.
3. Benjamin M, Evans EJ, Copp L. The histology of tendon attachment to bone in man. *J Anat* 1986;149:89-100.
4. Benjamin M, Moriggl B, Brenner E, Emery P, McGonagle D, Redman S. The "enthesis organ" concept: Why enthesopathies may not present as focal insertional disorders. *Arthritis Rheum* 2004;50:3306-3313.
5. Yasuda K, Kondo E, Ichiyama H, et al. Anatomic reconstruction of the anteromedial and posterolateral bundles of the anterior cruciate ligament using hamstring tendon grafts. *Arthroscopy* 2006;20:1015-1025.
6. Ferretti M, Ekdahl M, Shen W, Fu FH. Osseous landmarks of the femoral attachment of the anterior cruciate ligament: An anatomic study. *Arthroscopy* 2007;23:1218-1225.
7. Takahashi M, Doi M, Abe M, Suzuki D, Nagano A. Anatomical study of the femoral and tibial insertions of the anteromedial and posterolateral bundles of human anterior cruciate ligament. *Am J Sports Med* 2006;34:787-792.
8. Amis AA, Jakob RP. Anterior cruciate ligament graft positioning, tensioning and twisting. *Knee Surg Sports Traumatol Arthrosc* 1998;6:S2-S12 (Suppl 1).
9. Bernard M, Hornung H, Cierpinski T. Femoral insertion of the ACL. Radiographic quadrant method. *Am J Knee Surg* 1997; 10:14-22.
10. Colombet P, Robinson J, Christel P, et al. Morphology of anterior cruciate ligament attachments for anatomic reconstruction: A cadaveric dissection and radiographic study. *Arthroscopy* 2006;22:984-992.
11. Girgis FG, Marshall JL, Monajem A. The cruciate ligaments of the knee joint. Anatomical, functional and experimental analysis. *Clin Orthop Relat Res* 1975:216-231.
12. Giron F, Cuomo P, Aglietti P, Bull AM, Amis AA. Femoral attachment of the anterior cruciate ligament. *Knee Surg Sports Traumatol Arthrosc* 2006;14:250-256.
13. Harner CD, Baek GH, Vogrin TM, Carlin GJ, Kashiwaguchi S, Woo SL. Quantitative analysis of human cruciate ligament insertions. *Arthroscopy* 1999;15:741-749.
14. Mochizuki T, Muneta T, Nagase T, Shirasawa S, Akita KI, Sekiya I. Cadaveric knee observation study for describing anatomic femoral tunnel placement for two-bundle anterior cruciate ligament reconstruction. *Arthroscopy* 2006;22:356-361.
15. Keating AP, Knox J, Bibb R, Zhurov AI. A comparison of plaster, digital and reconstructed study model accuracy. *J Orthod* 2008;35:191-201.
16. Moritomo H, Goto A, Sato Y, Sugamoto K, Murase T, Yoshikawa H. The triquetrum-hamate joint: An anatomic and in vivo three-dimensional kinematic study. *J Hand Surg Am* 2003;28:797-805.
17. Purnell ML, Larson AI, Clancy W. Anterior cruciate ligament insertions on the tibia and femur and their relationships to critical bony landmarks using high-resolution volume-rendering computed tomography. *Am J Sports Med* 2008;36:2083-2090.
18. Shino K, Nakata K, Nakamura N, et al. Anatomic anterior cruciate ligament reconstruction using two double-looped hamstring tendon grafts via twin femoral and triple tibial tunnels. *Oper Tech Orthop* 2005;15:130-134.
19. Hutchinson MR, Ash SA. Resident's ridge: Assessing the cortical thickness of the lateral wall and roof of the intercondylar notch. *Arthroscopy* 2003;19:931-935.

内側半月板水平断裂の膝屈伸における変位・変形のMRI 3次元動態解析

天野　大[※1]　中田　研[※2]　岩橋　武彦[※2]　鈴木　智之[※3]
前　達雄[※2]　中村　憲正[※2]　菅本　一臣[※4]　吉川　秀樹[※2]
史野　根生[※5]

In vivo 3-D Dynamic MRI Evaluation of Movement, Deformation of Meniscus with Horizontal Tear.

Hiroshi AMANO, MD., Ken NAKATA, MD. PhD., Takehiko IWAHASHI, MD. PhD., Tomoyuki SUZUKI, MD., Tatsuo MAE, MD. PhD., Norimasa NAKAMURA, MD. PhD., Kazuomi SUGAMOTO, MD. PhD., Hideki YOSHIKAWA, MD. PhD., Konsei SHINO, MD. PhD.

Abstract

This study quantitatively evaluated the three-dimensional deformation and movement of the horizontally-torn menisci during knee flexion.

Nine knees with horizontally-torn medial menisci were analyzed using 3-D MRI from 0 to 60 degrees of flexion in 20-degree increments. Serial images were segmented to produce 3-D models of each knee angle. After matching each 3-D models of tibia using the volume-based registration method, three-dimensional deformation and movement of the meniscus during knee flexion were visualized and quantitatively evaluated.

Four of nine torn menisci with tear sizes in the horizontal plane exceeding more than 40% of the circumferential length showed different deformation patterns than those of normal menisci and their gaps opened by more than 2 mm with flexion. Other tears measuring less than 30% of the circumferential length opened by no more than 2 mm and showed movement and deformation patterns similar to those of normal menisci during flexion.

Horizontal tear more than 40% in circumferential length showed paradoxical movement and deformation, and opened by more than 2 mm with knee flexion.

Key words : 3-D MRI, Movement and deformation of meniscus, medial meniscus with horizontal tear.

※ 1　市立豊中病院　整形外科
〒560-8565　大阪府豊中市柴原町4-14-1

※ 2　大阪大学大学院　医学系研究科器官制御外科
〒565-0871　吹田市山田丘2-2
※ 3　札幌医科大学　整形外科
〒060-8556　札幌市中央区南１条西17丁目
※ 4　大阪大学大学院　医学系研究科運動器バイオマテリアル学
〒565-0871　吹田市山田丘2-2
※ 5　大阪府立大学　総合リハビリテーション学部
〒583-8555　羽曳野市はびきの3-7-30

Corresponding Author : Hiroshi AMANO, MD.
Department of Orthopaedic Surgery Toyonaka Municipal Hospital
4-14-1, Shibahara-cho, Toyonaka, Osaka 560-0055, Japan
Tel : +81-6-6843-0101　Fax : +81-6-6858-3531
E-mail address : h-amano@umin.ac.jp

はじめに

半月板の機能については，1948年にFairbankらが半月板の荷重分散機能について報告[6]して以来，関節安定性や関節潤滑，衝撃吸収，関節固有感覚への関与などが報告されている[1),11)]．膝屈伸時には，大腿骨と脛骨の動きに合わせて半月板が動くことで関節適合性が維持され，膝屈伸時にもこれらの機能をはたすことができている[8),10),12)]．

近年，MRIを用いた正常半月板の動態解析の報告がされている．Thompsonらは屍膝を用いて，膝屈曲に伴い半月板は後方へ移動し，内側半月板に比べ外側半月板が大きく動くと報告している[13)]．またVediらは生体膝を垂直型のopen MRIにて撮影し，立位荷重時には非荷重時に比べて半月板の移動量が大きくなることを報告している[15)]．

一方で，Boxheimerらは損傷半月板の動態解析について，垂直型openMRIを用いて報告している[3)]．その中で，環状断面では縦断裂と横断裂，complex tearで膝屈曲と回旋を加えたときに半月板が外側にdisplaceし，水平断裂ではあまりdisplaceしなかったと述べている．しかし，水平断裂は後節から後角に損傷の多く，膝屈伸による変位，変形は環状断面よりも矢状断面のほうが観察できると考えられるが，水平断裂を伴った半月板の動態を矢状断面で詳細に検討している報告はない．

そこで我々は，症状のある内側半月板水平断裂の膝関節屈伸に伴う変位・変形と損傷部の大きさを，３次元（3-dimentional, 3-D）MRIと3-Dコンピューターモデルを用いて定量評価し，病態について検討した．

対　象

内側半月板にMRIで水平断裂（Mink grade 3）を認め，半月板由来と考えられる症状を有し，水平断裂以外の損傷形態がなく，半月板以外の膝関節内および膝周囲に異常がない症例を対象とした．これらの条件に合致した９名９膝であった．男６例女３例で，平均年齢39.7歳（17～50歳）であった．

全例に本研究についての説明を十分に行いinformed consentを得た．

方　法

1．MRI撮影

MRIの撮影は，1.5TのMRシステム（MAGNETOM Espree, SIEMENS, Erlangen, Germa-

ny）と膝用コイル（伸展位：CP Extremity, SIEMENS, Erlangen, Germany, 屈曲位：Loop Coil, SIMENS, Erlangen, Germany）を使用した．この装置はガントリー径が70cmと大きく，膝屈曲位でも撮影が可能である．撮影条件はtrue FISP（Fat suppression water excitation, TR 9.77ms TE 4.33ms, Flip angle 28deg., FOV 16cm～20cm, slice厚0.8mm, matrix 320×256, slice resolution 50%, Band width 300hz/pixel, 撮影時間6分）を使用した．この撮影方法は軟骨や半月板と水分との分離が良いとされている[5),14)]．撮影は仰臥位で行い，専用のデバイスを用いて下腿内外旋は制限せず，膝関節伸展0度から屈曲60度まで20度刻みに4ポジションを撮影した（図1）．

2．3-D半月モデルの作成と半月板3-D動態の可視化

3-D半月モデルの作成と可視化には開発した解析ソフトVirtual Place-M（AZE Ltd., Tokyo, Japan）を用いた．MR画像から半月，脛骨，関節軟骨の輪郭をコンピューター上で半自動的に抽出し[9)]，3-Dコンピューターモデルを作成した（図2－(A)）．

Volume-based registration method[4)]を応用し，各屈曲角度で撮影した脛骨を画像の輝度値を基にコンピューター上で重ね合わせることにより，脛骨に対する異なる膝屈曲角度での半月板の3次元的空間位置を求めた．これらのデータを基に，関節運動に伴う3-D半月モデルの三次元動態を可視化した[16)]（図2－(B)）．

3．内側半月板水平断裂の膝関節屈伸に伴う変位・変形の定量評価

半月板水平断裂の膝屈伸に伴う変位・変形を定量評価するために，脛骨後縁の接線と直行し，脛骨の最大前後径となる傍矢状断面での断面を作成した（図3－(A)）．作成した傍矢状断面で見られる半月板の特徴点10点を以下のように設定した．前節は脛骨側付着部A，遊離縁B，大腿骨側縁C，後節は遊離縁D，脛骨側付着部E，大腿骨側縁Fとし，水平断裂部の脛骨面前縁G，脛骨面後縁H，断裂の滑膜移行部遠位縁I，断裂の滑膜移行部近位縁Jとした（図3－(B)）．

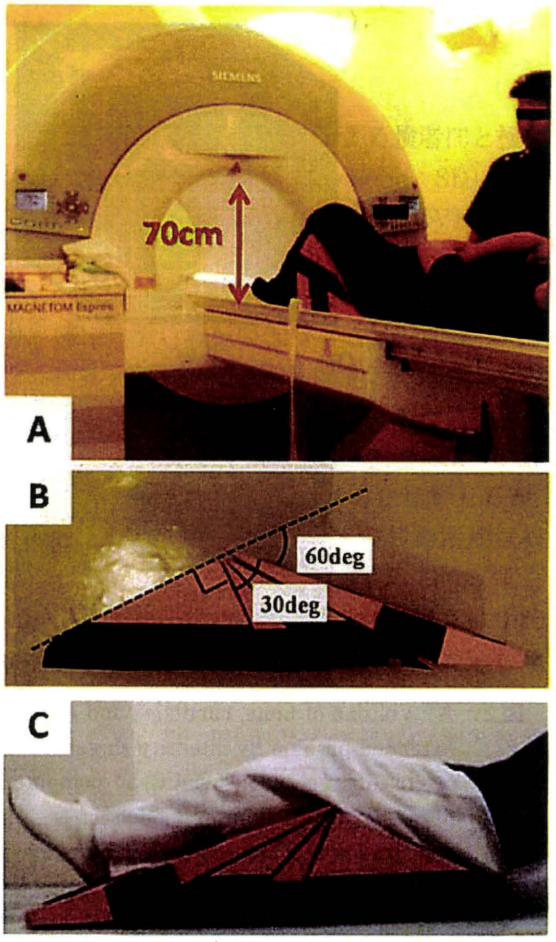

図1．A：1.5T MR scanner which is characterized by an expanded 70cm bore diameter.
B, C：A custom-made brace.

次に，Boxheimerらの報告に基づき[2)]，作成した傍矢状断面に脛骨高原皮質骨の接線HTRL（Horizontal tibial reference line）と，HTRLに直行し脛骨関節軟骨の前縁を通るATRL（Anterior tibial reference line）の2本を補助線として加えた．そして，HTRLとATRLから各特徴点までの距離をそれぞれの肢位で測定し，0度から60度までの変化量（移動距離）を計算した（図3－(B)）．半月板損傷部での屈曲に伴う変形の評価は，屈曲に伴うGH間距離の変化（水平方向の変化）とIJ間距離の変化（垂直方向の変化）を計算した．また，半月板後節を三角形に単純化することにより，それぞれの屈曲角度における水平断裂の損傷部面積（S）を特徴点E，G，H，I，Jの測定値から近似した．

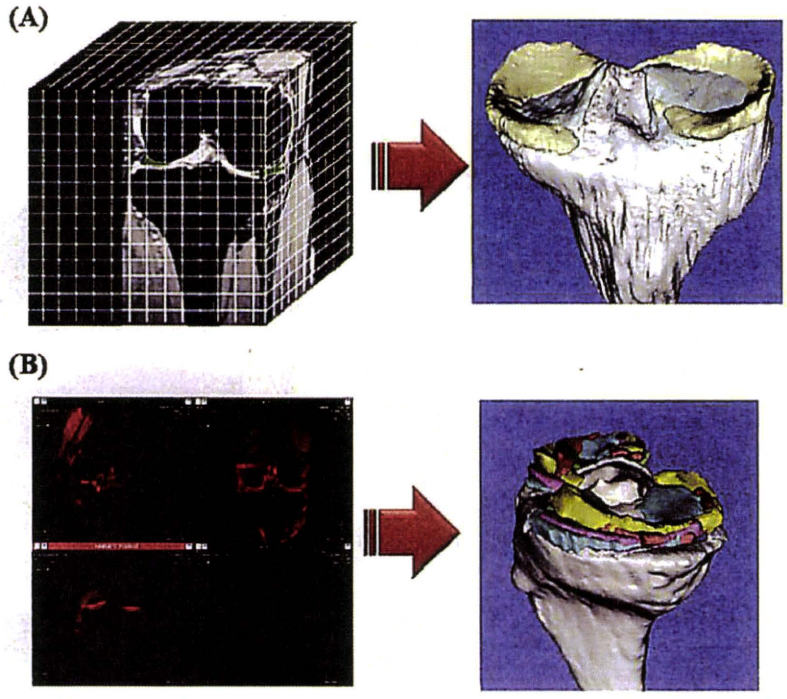

図2．A：Volume of bone, cartilage, and meniscus was semiautomatically extracted from the images of extended position by intensity threshold techniques to segment bony, cartilage and meniscal regions of tibia. Three dimensional (3-D) computer models then constructed using the marching cubes technique. B：3-D computer models of each position were automatically superimposed using volume registration technique, which is an image-processing method for matching volume images based on voxel values, and were visualized by the Visualization Tool Kit (VTK, Kitware Inc. New York, USA).

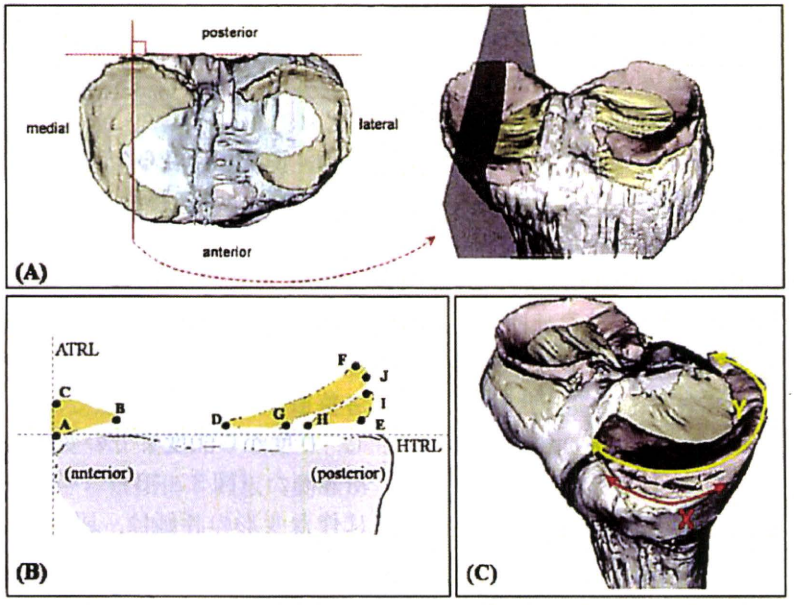

図3．A：3-D model of the knee was cut in the sagittal plane which crosses the most posterior part of the medial tibial plateau. B：Ten points A-J were chosen to evaluate movement and deformation of the meniscus body. C：The circumferential length of horizontal tear was also measured against the whole circumferential length of meniscus on the 3-D meniscus models.

三角形JGEの面積から三角形IEHの面積を引くことにより，損傷部面積の近似値を計算した（S@0°，S@20°，S@40°，S@60°）．伸展0度から屈曲60度までの変化量（⊿S＝S@60°－S@0°）を評価した．

内側半月水平断裂の損傷部の広がりを評価するため，半月辺縁部の損傷部の円周方向の長さ（X）と，半月の円周方向の全長（Y）の比（X/Y）を% tearとして評価した（図3－(C)）．

4．測定における信頼性

半月板の特徴点10点の位置を，同一検者による3回の測定と，3人の検者による各1回の測定から，検者内あるいは検者間の標準偏差（stadard deviation：SD）と変動係数（coefficients of variation：CV），級内相関係数（intraclass correlation coefficient：ICC）を計算した．信頼性を評価したのちに，同一検者により半月板の特徴点10点を測定した．

5．統計処理

統計ソフトはSSPS11.5J（SSPS Japan Inc. Tokyo, Japan）を使用した．相関係数はSpearmanの順位相関係数より求め，$p<0.05$を有意とした．

結　果

1．測定における信頼性

半月板特徴点10点の測定による検者間と検者内の標準偏差（standard deviation：SD）と変動係数（coefficients of variation：CV），級内相関係数（intraclass correlation coefficient：ICC）を表1に示す．ICCはいずれも0.99であり，測定における信頼性は高いといえる．

2．内側半月板水平断裂の膝屈曲に伴う変位，変形

後節に水平断裂のある内側半月板は，膝屈曲に伴い，前節と後節とも9例全例で後方に移動した．前節のA，B，C点は後方に移動したが，A，B，C点それぞれの後方への移動距離は異なり，A点平均4.7mm，B点平均6.8mm，C点平均6.6mm後方へ移動し，C点の高さは平均0.2mm低くなり，前節は屈曲に伴い変形を呈した．後節のD，E，F点も9例全例で後方へ移動したが，D，E，F点それぞれの後方移動距離は異なり，D点平均4.8mm，E点平均4.2mm，F点平均4.6mm後方に移動し，F点の高さは平均1.8mm高くなり，後節も屈曲に伴い変形を呈した（図4－(A)，(B)）．

表1．The intra-observer and inter-observer standard deviation (SD), coefficients of variation (CV) and intraclass correlation coefficient (ICC) for ten points.

膝屈曲角度	特徴点	検者間			検者内		
		SD (cm)	CV (%)	ICC	SD (cm)	CV (%)	ICC
0°	A	0.00	0.00	0.99831	0.00	0.00	0.99938
	B	0.00	0.00		0.06	5.41	
	C	0.06	10.83		0.06	10.19	
	D	0.10	4.35		0.00	0.00	
	E	0.10	2.13		0.06	1.26	
	F	0.06	5.97		0.00	0.00	
	G	0.12	3.43		0.06	1.67	
	H	0.06	1.53		0.06	1.57	
	I	0.06	17.32		0.00	0.00	
	J	0.00	0.00		0.00	0.00	
60°	A	0.15	41.66	0.99753	0.00	0.00	0.99938
	B	0.12	7.37		0.00	0.00	
	C	0.00	0.00		0.00	0.00	
	D	0.06	2.37		0.06	2.34	
	E	0.06	1.19		0.06	1.19	
	F	0.10	7.69		0.00	0.00	
	G	0.06	1.62		0.06	1.62	
	H	0.06	1.43		0.00	0.00	
	I	0.06	13.32		0.06	15.75	
	J	0.06	7.53		0.06	7.87	

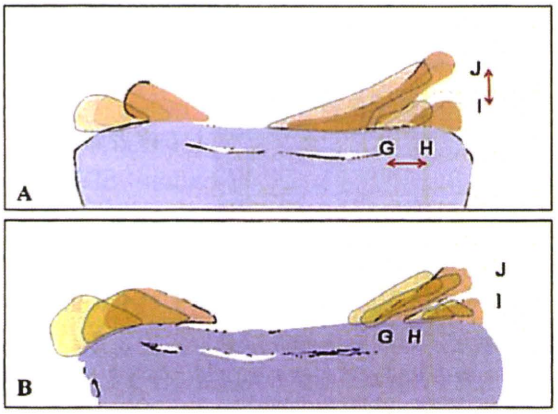

図4．Deformation of horizontal tear of medial meniscus. A : case1. The distance GH (horizontal gap) and IJ (vertical gap) increased during knee flexion. B : case2. The gap of tear is hardly opened during knee flexion.

3．損傷部の膝屈曲に伴う変形

膝屈伸に伴う損傷部の変位，変形の変化と損傷部の大きさを示す（表1）．

水平方向GH間の膝屈曲による変化は，個々の症例により異なり－1 mmから4 mmで，9例平均では1.0mmと開大した．損傷部の垂直方向IJも症例により異なり，0 mmから4 mmで，9例平均で平均1.6mm開大した（図4－(A)，(B)，表2）．また，これらGH間の距離変化とIJ間の距離変化の間には，強い正の相関関係を示した（$R^2=0.8$，$p<0.01$，図5－(A)）．

表2．Results of the change of distance of GH and IJ, the % tear, and the change of tear site area (⊿S).

n	年令	GH間距離変化(mm)	IJ間距離変化(mm)	%tear(%)	⊿S(mm²)
1	39	3	3	47.7	19
2	30	1	3	50.2	14
3	50	0	1	28.0	0
4	47	-1	0	20.1	5.5
5	44	0	0	20.5	0.5
6	41	0	1	23.0	-0.5
7	42	2	2	41.5	16
8	47	0	0	16.9	-4.5
9	17	4	4	52.5	19.5
平均	39.7	1.0	1.6	33.4	7.7
SD	10.3	1.7	1.5	14.4	9.4

4．損傷部面積と三次元半月モデルによる内側半月水平断裂の損傷部の大きさ

三次元半月モデルでは，内側半月水平断裂が辺縁部の間隙として認められ，% tearは16%から52%であった．損傷部の大きさの分布は，30%以下の例が5例，40%を越える例が4例であった（表2）．

また，膝伸展から屈曲60度までの損傷部面積の変化量は$-4.5mm^2$から$19.5mm^2$であった（表2）．

損傷部の大きさ% tearと，損傷部面積Sの膝屈伸による変化の間には，高い正の相関を認め相関係数は0.8857（$p<0.01$）であった．つまり，損傷部の大きさが大きな症例は損傷部が膝屈曲

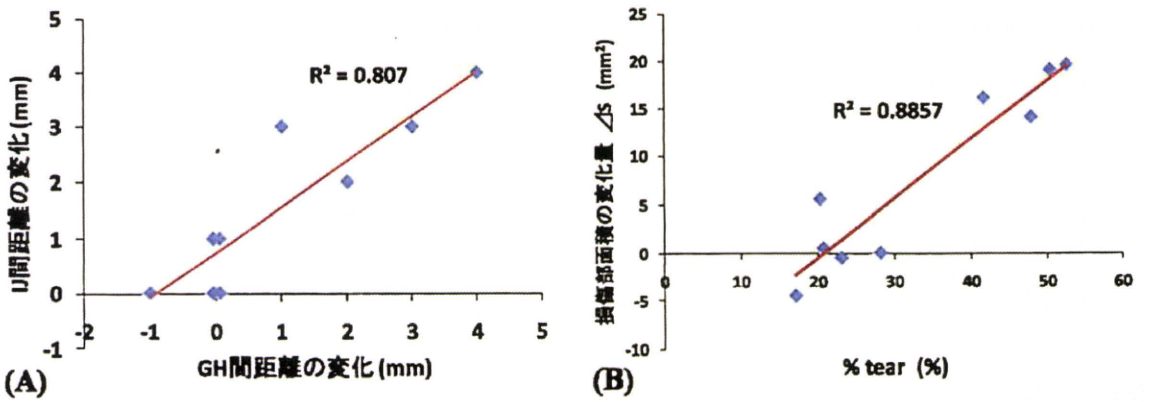

図5．A : Scatter plots of the change of GH versus IJ with best-fit line. B : Scatter plots of the % tear versus the change of tear site area with best-fit line.

に伴って開大する症例であった（図5－(B)）.

考　　察

われわれは症状のある水平断裂の膝屈曲に伴う変位，変形を，3-DMRIおよび3-Dコンピューターモデルにより検討した．本研究の特徴は，屍膝ではなく生体での3-D動作解析という点であり，さらにbore径の広いMRIを用いることで，従来のMRIでは撮影が制限されていたような機能的な肢位での撮影が可能となった．また，volume-based registration method[4]を応用し，各屈曲角度で撮影した脛骨を画像の輝度値を基にコンピューター上で重ね合わせることにより，脛骨に対する異なる膝屈曲角度での半月板の3次元的空間位置を求める本手法は，位置誤差，回転誤差1mm，1度以下の高精度なシステムであり[16]，従来法に比べより生理的かつ正確な動作解析が可能となる．

MRIによる正常半月板の変位に関して，過去にいくつか報告されている．Thompsonらは新鮮凍結膝5膝を用いて膝伸展0度から屈曲120度までを調べ，内側半月板前節は7.0mm，後節は3.2mm後方へ変位し，外側半月板前節は12.8mm，後節は9.6mm後方へ変位すると報告している[13]．またVediらは生体膝を垂直型open MRIにて撮影し，立位荷重時には非荷重時に比べて半月板の移動量が大きくなることや，高さ変化において荷重により外側半月板前角では変化が大きいが，内側半月板ではあまり変わらないことを報告している[15]．本研究でも，変位についてはこれら正常半月板の報告と同様に，膝屈曲に従い後方へ変位していた．

一方で，損傷半月板の変位，変形についてはBoxheimerらが報告している[3]．垂直型open MRIを用いて，非荷重伸展位から屈曲90°，荷重，内外旋を加えて，環状断面での半月板のdisplaceについて検討している．それによると，縦断裂，横断裂，complex tearはdisplaceが大きく，水平断裂はdisplaceが小さかった，と述べている．しかし，水平断裂は損傷部位が後節から後角に存在することが多いため，環状断面よりも矢状断面で変位，変形が大きくなると考えられる．したがってわれわれは，水平断裂について，3-DMRIの矢状断像と3-Dコンピューターモデルから病態を検討し，屈曲に従い損傷部が開大する症例が存在することを明らかにした．

内側半月水平断裂の3-D半月モデルでは，辺縁部の間隙として損傷部が示され，今回計測した9例では症例により水平方向の広がりが異なっていた．半月板全周に対する損傷部の割合である％tearが30％以下の症例が9例中5例であり，40％以上の症例が9例中5例であった．言い換えれば，同じ症状を有する水平断裂であっても，損傷の大きさは異なっていた．また，％tearと膝屈曲に伴う損傷部面積の変化の間には高い正の相関関係がみられた．つまり，損傷部が大きいものが損傷部の開大が大きいことが明らかになった．本研究では検討していないが，損傷部の開大は関節包に無理な力が生じ，疼痛の原因になりうるのではないかと考えられる．臨床症状との検討は今後の課題である．

HaugerらはMRIの半月板像と半月板を比較し，MRI画像でのWedge shapeの信号域が半月全体を描出していると報告している[7]ことから，MR画像上で半月板を同定することは十分な精度を持って可能であると考えられる．また，本研究のMRI撮影の条件はtrue FISPを採用している．この撮影条件はVasanawalaらが報告している[10]ように軟骨，半月，関節液との分離が非常に判定しやすく，損傷部の特定も容易である．さらに，3-Dモデルの作成と測定部位決定での信頼性は，われわれが3検者で検討したところ検者内，検者間ともにICC＞0.99と十分高いと考えられる．しかし生体の半月板と3Dモデルの半月板との精度評価については，半月板は非剛体であるため困難であり今後の課題である．

本研究の限界については，非荷重下の静止画像であること，また膝屈曲が60度までであり深屈曲していない点があげられる．より生理的な環境を再現するには，荷重下に連続運動として画像化することが望ましい．今後，MR撮影室内で使用可能な荷重装置の開発や，撮影時間の短縮が必要である．

しかし，3-D MR撮影から3-D半月モデルを作製することで，形態的な検討がより詳細にでき，異なった肢位で撮影することで，生理的に近い関節運動が視覚化され再現できる．これにより，半月損傷の病態を詳しく理解することにつながると考えられる．また，この手法を用いれば，半月損傷の治療効果を形態的評価だけでなく機能的評価も可能となる可能性があり，今後有用になっていく方法であると考えられる．

結　　論

膝屈伸による内側半月板水平断裂の三次元動態MRI解析を９例９膝で行なった．水平断裂を持つ内側半月板も９例全例で膝伸展から屈曲60°まで後方に変位し，変形していた．水平半月損傷部の変形は症例により異なり，膝屈曲により損傷部は水平方向に－１mmから４mmまで変化し，垂直方向は０mmから４mmまで変化した．また，損傷部の大きさと損傷部の断面積の膝屈曲による変化量は正の相関を示しており，損傷部が大きいと損傷部は大きく開大することがわかった．

文　　献

1）Bessette GC. : The meniscus. Orthopedics 15 : 35-42, 1992.

2）Boxheimer L, Lutz AM, Treiber K, et al. : MR imaging of the knee : position related changes of the menisci in asymptomatic volunteers. Invest Radiol. 39 : 254-63. 2004.

3）Boxheimer L, Lutz AM, Weishaupt D, et al. : Characteristic of displaceable and nondisplaceable meniscal tears at kinematic MR imaging of the knee. Radiology. 238 : 221-31. 2006.

4）Brown LG. : A survey of image registration techniques. ACM Compt Surveys. 24 : 325-76. 1992.

5）Duc SR, Hodler J, et al. : Articular cartilage defects detected with 3D water-excitation true FISP : prospective comparison with sequences commonly used for knee imaging. Radiology. 245 : 216-223, 2007.

6）Fairbank TL. : knee joint changes after menisectomy. J Bone Joint Ssurg. 30B : 664-670, 1948.

7）Hauger O, Resnick D, et al. : Characterization of the "Red zone" of knee meniscus : MR imaging and histologic correlation. Radiology. 217 : 193-200, 2000.

8）Hsieh HH, Walker PS. : Stabilising mechanisms of the loaded and unloaded knee joint. J Bone Joint Surg. 58A : 87-93, 1976.

9）Lorensen W, Cline H. : Marching cubes : a high resolution 3D surface construction algorithm. Comput Graphics. 21 : 163-9. 1987.

10）Markolf KL, Amstutz HC, et al. : Stiffness and laxity of the knee. The contributions of the supporting structures : a quantitative in vitro study. J Bone Joint Surg. 58A : 583-94, 1976.

11）McBride ID, Reid JG. : Biomechanical considerations of the menisci of the knee. Can J Sport Sci. 13 : 175-87, 1988.

12）Seedhom BB. : Transmission of the load in the knee joint with special reference to the role of the menisci. Part 1 : anatomy, analysis and apparatus. Engineering in Medicine. 8 : 207-28, 1979.

13）Thompson WO, Fu FH, et al. : Tibial meniscal dynamics using three-dimensional reconstruction of magnetic resonace images. Am J Spots Med. 19 : 210-215, 1991.

14）Vasanawala SS, Gold GE, et al. : Rapid musculoskeltal MRI with phase-sensitive free precession : comparison with routine knee MRI. Am J Roentgenol. 184 : 1450-1455, 2005.

15）Vedi V, Tennat SJ, et al. : Meniscal movement. J Bone Joint Surg. 81B : 37-41, 1999.

16）Yamada Y, Toritsuka Y, Shino K, et al. : Morphological analysis of the femoral trochlea in patients with recurrent dislocation of the patella using three-dimensional computer models. J Bone Joint Surg Br 89 : 746-751. 2007.